

Assessing the dual radiative consequences of urban PV integration Albedo change and radiative forcing dynamics

Zhou, Yilong; Marathe, Shredatta; Zeman, Miro; Isabella, Olindo; Ziar, Hesan

DO

10.1016/j.apenergy.2025.126544

Publication date

Document VersionFinal published version

Published in Applied Energy

Citation (APA)

Zhou, Y., Marathe, S., Zeman, M., Isabella, O., & Ziar, H. (2025). Assessing the dual radiative consequences of urban PV integration: Albedo change and radiative forcing dynamics. *Applied Energy*, 401, Article 126544. https://doi.org/10.1016/j.apenergy.2025.126544

Important note

To cite this publication, please use the final published version (if applicable). Please check the document version above.

Copyright

Other than for strictly personal use, it is not permitted to download, forward or distribute the text or part of it, without the consent of the author(s) and/or copyright holder(s), unless the work is under an open content license such as Creative Commons.

Takedown policy

Please contact us and provide details if you believe this document breaches copyrights. We will remove access to the work immediately and investigate your claim.

ELSEVIER

Contents lists available at ScienceDirect

Applied Energy

journal homepage: www.elsevier.com/locate/apen



Assessing the dual radiative consequences of urban PV integration: Albedo change and radiative forcing dynamics

Yilong Zhou*, Shredatta Marathe, Miro Zeman, Olindo Isabella o, Hesan Ziar o

Photovoltaic Materials and Devices (PVMD) Group, Delft University of Technology, Mekelweg 4, Delft, 2628CD, South Holland, the Netherlands

HIGHLIGHTS

- · A LiDAR-based workflow is developed to quantify urban albedo and radiative forcing (RF).
- The albedo results are validated with MODIS product, showing 6.12 % absolute difference.
- Roof PV in Delft lowers the city's albedo (minimal -0.0306), imposing 3.53×10^{-8} W/m² positive RF.
- • Roof PV in Delft yields 485.72 GWh/year, offsetting positive RF by reducing ${\rm CO_2}$ emissions.
- · The offset time is around forty days and increases as the energy infrastructure decarbonizes.

ARTICLE INFO

Dataset link: Code for evaluating albedo change and radiative forcing from roof PV integration in Delft (Original data)

Keywords: Albedo Urban solar photovoltaics Radiative forcing Large-scale simulation

ABSTRACT

Integrating photovoltaic (PV) systems in urban areas enhances local renewable electricity production but also reduces surface albedo due to the lower reflectivity of PV panels. This albedo reduction increases Earth's energy absorption, resulting in positive radiative forcing (RF), while the displacement of fossil fuels by PV electricity leads to negative RF through avoided CO_2 emissions. This study quantifies the net RF impact of urban rooftop PV deployment using a novel workflow. This proposed workflow combines: (1) a geometric spectral albedo (GSA) model, using LiDAR data and geo-referenced material maps to simulate albedo changes before and after PV integration; and (2) a simplified skyline-based PV model, using LiDAR-derived roof geometry to estimate annual PV electricity generation. The method is applied to the city of Delft, the Netherlands, and the average simulated albedo of Delft is 0.1584, differing by 6.12 % from MODIS observations (0.1493). Full PV integration on all rooftops reduces the city-wide albedo to 0.1557, corresponding to a positive RF of $3.53 \times 10^{-8} \text{ W/m}^2$. This can be offset in about 40 days by negative RF from PV electricity, assuming a grid carbon intensity of 454 gCO₂-eq/kWh. However, under a low-carbon grid scenario (30 gCO₂-eq/kWh), the payback time increases to 623 days, indicating that positive RF from albedo reduction becomes more relevant in future decarbonized scenarios. This study contributes to understanding the climatic implications of urban PV deployment and offers insights into the realistic potential of PV systems in mitigating climate change.

1. Introduction

As a major pillar of renewable energy, photovoltaics (PV) is playing a key role in the long-term decarbonization strategy established in the Paris Agreement that aims at limiting global warming to 1.5 °C [1,2]. In support of this goal, countries worldwide are making substantial commitments to expand renewable energy infrastructure. In 2024 alone, global renewable power capacity increased massively by 585 GW, of which solar PV contributed 451.9 GW [3]. China has taken a leading role, adding 278 GW of new solar capacity, which accounts for nearly

62 % of the global PV expansion. Although PV currently accounts for a relatively small share of global electricity generation (5.5 % as of 2023), significant growth is anticipated [4]. This growth is driven not only by continuous technology development and cost reduction, but also by improved regulations that simplify permitting processes for renewable energy projects and by a growing number of national net-zero strategies that prioritize PV as a core component in decarbonization efforts [5,6]. A recent study predicts an annual PV growth rate of 25 %, and the worldwide installed PV capacity will reach up to 75 TW by 2050

^{*} Corresponding author.

Email address: Y.Zhou-15@tudelft.nl (Y. Zhou).

Nomenclature

Abbreviations

ASTER Advanced spaceborne thermal emission reflection

radiometer

BIPV Building-integrated photovoltaic
DHI Diffuse horizontal irradiance
DNI Direct normal irradiance
DSM Digital surface model
ET Equilibrium time

GSA Geometric spectral albedo

GW Gigawatt

LCA Life cycle assessment
LiDAR Light detecting and ranging

LOS Line-of-sight

MODIS Moderate resolution imaging spectroradiometer

PV Photovoltaic RF Radiative forcing RMS Root mean square

SMARTS Simple model of the atmospheric radiative transfer of

sunshine

STC Standard test conditions

SVC Sky view factor
SCF Sun coverage factor
TMY Typical meteorological year

TW Terawatt

TOP Top of the atmosphere UHI Urban heat islands

Symbols

 α_t Temporal albedo

 R_i Reflectivity of differential section i R_{λ} Directional hemispherical reflectance

 $F_{S \to Ai1}$ View factor of differential section A_{i1} to the albedometer S

 $F_{S \to Ai2}$ View factor of differential section A_{i2} to the albedometer S C_i Chance factor of section i illuminated and visible to albedometer S

 C'_i Chance factor of section i shaded and visible to albedometer S

 G_{λ} Hourly clear sky spectral irradiance

 G_{TMY} Hourly GHI from Meteonorm TMY

 $G_{SMARATS}$ Hourly GHI derived by integrating the SMARTS spectral data

x, y, z Coordinates of the DSM points

 ψ Hourly azimuth of the Sun

 θ Hourly altitude of the Sun

u, v, q, p Coordinates in the new UQV and UQP system

 δ_u , δ_q Grid size along U and Q axes d_t Depth of the uppermost segment

 d_i Linear distance between the albedometer S and ground section i

 θ_i Angle between vector d_i and ground surface normal

r Roughness

 δ_{xi}, δ_{yi} Slopes along x and y directions

 $\bar{\delta}_{x}, \bar{\delta}_{y}$ Mean value of the slopes along x and y directions

 E_Y PV annual energy yield RF_n Positive radiative forcing

 K_m Radiative kernel for monthly climatological albedo changes

 $\Delta \alpha_m$ Albedo change

 A_{PV} Area of the pixels influenced by PV integration

 A_E Surface area of the Earth

 k_{CO_2} Radiative forcing induced by increasing unit kilogram of CO_2

 I_{carbon} Electricity carbon intensity

 E_{CO_2} Annual roof PV electricity generation

 IRF_{CO_2} Impulse-response function of decaying CO_2 concentration over time

 α_{bs} Black sky albedo

 α_{ws} White sky albedo

 f_{dif} Annual mean of hourly fraction of GHI to the extraterrestrial irradiance

[7]. One of the main contributors to this PV scenario will be distributed PV systems, especially considering the ongoing progress of urbanization [8]. Compared to the traditional utility–scale PV farms, distributed PV systems have several advantages, such as their ease of local implementation, no additional land use required, optimization of urban surface utilization, and being adjacent to the energy consumers [9,10]. In fact, the share of distributed PV in China's national installed PV capacity more than doubled between 2016 and 2020, increasing from 13 % to 31 %, and this trend is expected to continue to meet the long-term climate ambition [11,12]. Although the expansion of PV integration within urban settings enhances the local production of green electricity, it also gives rise to adverse effects that impact the environment [13]. These effects mainly result from alterations in the energy balance caused by the substitution of original urban surfaces with highly absorptive PV panels, which leads to a reduction in urban albedo [14].

On a local scale, this changed urban albedo significantly contributes to the formation of urban heat islands (UHI), increasing the urban air temperature. This elevation in temperature not only boosts building cooling energy demand but also degrades the thermal comfort of urban dwellers, adversely affecting their health and potentially reducing life expectancy [15]. In an early study modeling the impact of extensive PV deployment on urban air temperature within the Los Angeles Basin, Taha reported a cooling effect of 0.2 °C after retrofitting the roofs with PV panels of 30 % conversion efficiency [16]. In this analysis, the concept of effective albedo is used to quantify the albedo of PV panels, which essentially is the sum of reflectance and energy conversion efficiency of PV panels. This simplification is initially plausible as it accounts for the conversion of part of incident solar energy into electricity, which does

not directly contribute to local urban heating. However, this assumption may lead to inaccurate results since the conversion efficiency of PV panels is often lower than the one outlined under the standard test conditions (STC) [17,18]. Masson et al. simulated a scenario of PV deployment in the Paris metropolitan area, in which they discovered that PV panels reduce the UHI effect by 0.2 K during the day and 0.3 K at night [19]. Similarly, Salamanca et al. found a decreased near-surface air temperature following the implementation of PVs in the cities of Phoenix and Tucson [20]. However, both studies adopted the assumption that the temperature of the rear surface of PV panels is equal to the ambient air temperature. This assumption could be unreliable considering the small heat capacity of PV panels, meaning that the temperatures of the front and rear surfaces of PV panels should be closely aligned [21]. Cortes et al. performed a numerical simulation and reported a cooling effect of building integrated PVs (BIPVs) on urban air temperature, but the validity of these findings is debatable because the study used questionable assumptions that the albedo of PV cells is identical to that of the building envelope [22].

Contrasting conclusions have been reached by other studies suggesting that PV deployment may contribute to local warming. For instance, placing a large-scale PV array in the Mojave Desert of California can increase the local temperature by 0.4 °C when using the concept of PV effective albedo [23]. Complementary on-site measurements between the PV plant and adjacent wildlands observed that the temperatures above the PV plant are consistently warmer than wildlands by 3–4 °C [24]. Extending to the scenario of a densely populated city, Garshasbi et al. simulated the impact of PV deployment on air temperatures in Sydney during the summer months. The simulation indicated that

expanding the coverage of urban roofs with PV panels from 25 % to 100 % could raise ambient air temperatures by 0.6-2.3 °C, and this temperature increase was translated to a cooling load penalty of around 1.7 to 6.8 kWh/m² [25]. Similarly, a consistent effect was also reported at the local district scale of Sydney, where deploying solar panels raises the summer daytime air temperature by 1.5 °C while reducing the nighttime temperature by 2.7 °C [26]. This inconsistency in the local environmental effect of PV deployment can be mainly attributed to the reliance on simplified assumptions in the models to address the complex urban energy balance. These simplifications often include the use of a constant PV conversion efficiency, an underestimation of the convective heat exchange with the environment at the rear side of PV panels, and inaccurate albedo assignments for the surrounding landscape. By refining these assumptions and incorporating the overlooked mechanisms of heat exchange between PV panels and the environment, it is expected that the implementation of PV panels in urban settings can lead to local warming during the day and potentially a cooling effect at night [27].

On a global scale, albedo plays a crucial role in our planet's climate dynamics. The Earth continuously receives solar energy and radiates energy back to space. The balance between these energy flows is called radiative forcing (RF). Positive RF indicates that the Earth absorbs more energy than it radiates back to space, leading to the warming effect. while negative RF suggests the opposite. Globally, there are three primary factors influencing the RF and each of them is effective over different timescales: (i) variation in solar irradiation, such as the 11year sunspot cycle; (ii) volcanic activities that inject particles and gases into the atmosphere, temporarily reducing incoming solar radiation and typically influencing RF over a few years; and (iii) human activities, including fossil fuel combustion and land surface modification, which are currently recognized as the dominant drivers of global warming [28]. In the context of PV deployment, the integration of PV panels reduces albedo, thereby enhancing the positive RF and increasing the energy absorbed by the Earth [29,30]. Conversely, the deployment of PV panels displaces the use of fossil fuels, lowering the CO2 concentration in the atmosphere and contributing to negative RF. It is reported that the installation of solar farms can reduce the annual mean shortwave albedo by 0.007 to 0.025, depending on the background surface replaced by PV panels [31]. Although the temperature increase due to the unit square meters of albedo change is relatively minor, the extensive installation of highly absorptive PV panels would still lead to measurable global climate warming [32,33]. The fact that PV panels convert part of the incident solar energy into electricity redistributes the solar radiation received by the Earth, which alters the atmospheric circulation and influences regional and global climates. The majority of this generated electricity is consumed in urban areas and eventually is converted to heat, increasing the regional and global temperatures [34]. Nemet's research further quantified the positive RF resulting from albedo change due to PV deployment and compared it with the negative RF from the displacement of fossil fuels. It was determined that the RF avoided by replacing fossil fuels with PV is approximately 30 times greater than the effect induced by albedo modification [35].

These pioneering works have provided valuable insights into the role of PV in climate change mitigation, particularly by evaluating the positive RF caused by albedo reduction. However, many of these studies either neglect the negative RF resulting from fossil fuel displacement or estimate it using simplified assumptions or generalized PV yield calculation equations, especially at the urban scale, which may lead to inaccurate results. Additionally, the use of satellite data with coarse resolution, such as those from the Moderate Resolution Imaging Spectroradiometer (MODIS), poses significant challenges to assess the albedo modification before and after urban PV installation due to its spatial resolution, which is typically 500 m. While this resolution is generally suitable for large-scale solar farms—where the surface albedo can be reasonably approximated by replacing the pixel's original value with that of PV panels—it is insufficient for urban environments. Urban PV systems are small, distributed across complex built environments, and

often take up only a small fraction of each pixel. Therefore, pixel-level albedo replacement can be challenging for capturing the spatial variance of PV, leading to inaccurate estimates of albedo change. The objective of this work is to fill the research gap by introducing a high-resolution approach to quantify both positive and negative RF effects of distributed urban rooftop PV systems. Compared to earlier studies using satellite data or simplified equations, this work introduces two novel simulation frameworks that leverage Light Detecting And Ranging (LiDAR) data. The first framework is an albedo simulation tool that simulates surface albedo changes before and after PV deployment. The second framework involves a large-scale rooftop PV simulation model designed to calculate PV electricity generation. The Netherlands, specifically the city of Delft, is selected for this study due to the authors' comprehensive access to the high-resolution datasets required for the analysis. Both frameworks are built to accurately calculate the radiative impacts of roof PV integration. The outcomes from these two frameworks are further translated into positive and negative RFs to calculate the Equilibrium Time (ET) the duration required for the negative RF from PV electricity generation to completely offset the positive RF from albedo reduction.

2. Methodology

This section elaborates on the methods implemented in this study, which consist of three main steps: (1) albedo simulation, (2) PV electricity computation, and (3) RF calculation. An overview of the steps employed in this analysis is illustrated in the flowchart as shown in Fig. 1. Additionally, the simulated albedo results are validated with MODIS albedo products, and the collection of MODIS data is also elaborated upon. Table 1 provides a summary of the software used in this study, including their respective tasks and the average runtime. The configuration of the computer used in this project includes two AMD EPYC 7543 (32-core) processors running at a base frequency of 2.8 GHz and 128 GB of DDR4 RAM.

2.1. Geometric spectral albedo (GSA) model

The framework for albedo simulation was established based on the Geometric Spectral Albedo (GSA) model, which is a mathematical model incorporating the parameters influencing albedo such as geometry, material, and light source [38]. This model essentially decouples the upward radiation reflected from the surface into the contributions from shaded and unshaded differential sections, as illustrated in Fig. 2. In this representation, a hypothetical albedometer S is denoted. The shaded sections receive exclusively diffuse horizontal irradiance (DHI), while the unshaded sections are exposed to both DHI and direct normal irradiance (DNI). The distribution of the shading pattern is further influenced by the surface roughness, which causes self-shadowing in the unshaded area, thereby converting some sections from being unshaded to shaded. Additionally, surface roughness can also obstruct the path of reflected radiation, preventing it from traveling from one section to the albedometer and thus not contributing to the albedo. Consequently, reflected light from the surface contributes to the albedo only if it is visible to the albedometer, and the extent of this contribution is determined by the illumination condition, surface material reflectivity, and the view factor of the differential section relative to the albedometer.

The general equation for temporal albedo α_t calculation implemented in this study is as follows:

$$\alpha_{t} = \sum_{i=1}^{N} R_{i} \left(C_{i} F_{S \to A_{i1}} + \frac{1}{H+1} \left(C'_{i} F_{S \to A_{i1}} + F_{S \to A_{i2}} \right) \right)$$
 (1)

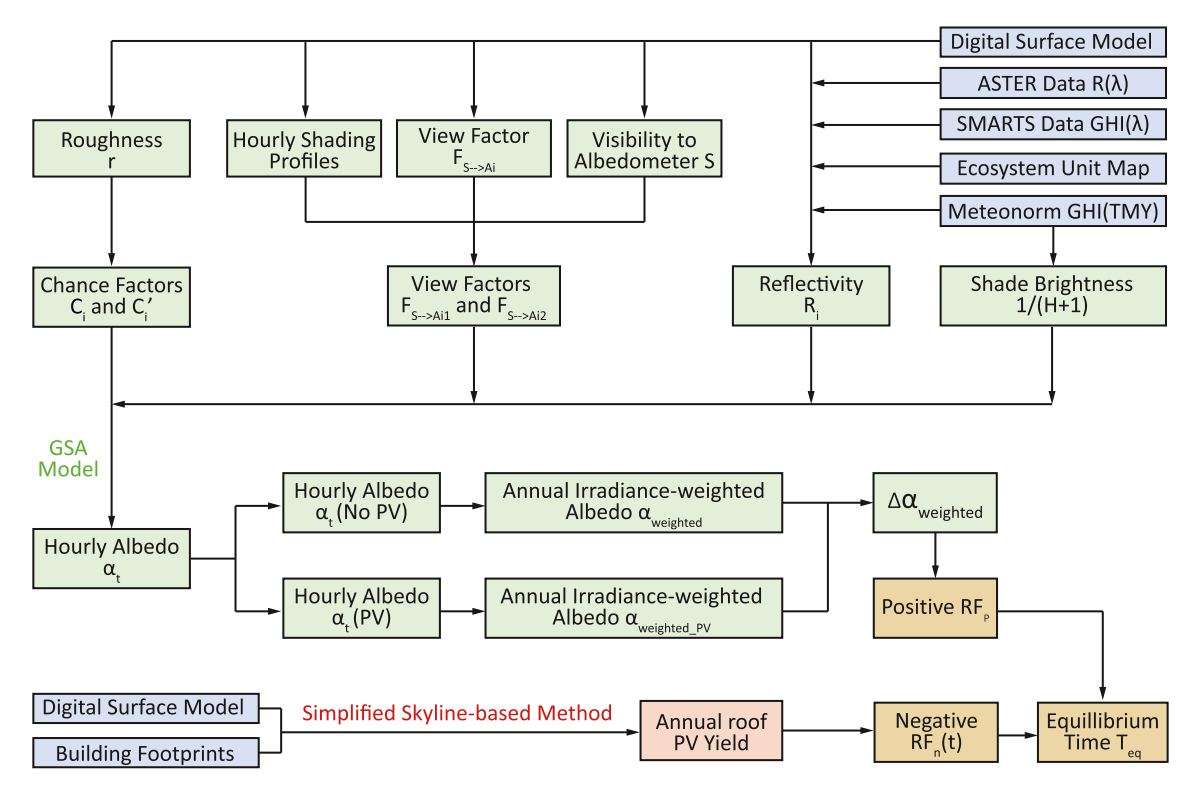


Fig. 1. Flowchart showing the steps adopted in this study to (i) simulate the albedo before and after rooftop PV integration (green blocks); (ii) to compute the annual rooftop PV yield (red block); (iii) to analyze the RFs induced by the rooftop integrated PV; and (iv) to calculate the equilibrium time at which the negative RF exceeds the positive RF (yellow blocks). The blue blocks represent the input data. ASTER, SMARTS, and TMY refer to Advanced Spaceborne Thermal Emission Reflection Radiometer, Simple Model of the Atmospheric Radiative Transfer of Sunshine, and Typical Meteorological Year, respectively [36,37].

Table 1
Software used in this study, including their respective tasks and average runtime. The reflectance of SUNPOWER PSR-X21-350 IBC c-Si solar cell is used as the reflectance for PV material.

| Software | Version | Task | Avg. runtime [min] |
|----------------------|-----------------|---|---|
| ArcGIS Pro MATLAB | 3.1.0 R2023a | DSM generation GSA albedo simulation Rooftop PV simulation RF calculation MODIS albedo processing | 1.0 per tile 77.6 per grid point 198.7 0.2 23.2 |

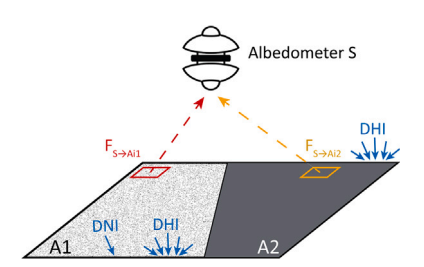


Fig. 2. Visual illustration of GSA model with a rough surface being partially shaded. The unshaded and shaded sections are denoted as A1 and A2, respectively. Section A1 is exposed to both DNI and DHI, while section A2 only receives DHI. The view factor of each differential section relative to the hypothetical albedometer is indicated by F. Surface roughness causes self-shadowing within section A1 and obstructs the travel of reflected radiation from the surface to the albedometer.

illuminated and visible to the albedometer due to self-shadowing; the chance factor C'_i , which represents the probability that a differential section is shaded yet visible to the albedometer due to self-shadowing;

and the variable H which is influenced by the sky condition and the Sun's position. These variables are determined by three primary factors: the material types, the terrain morphology, and the meteorological conditions

2.1.1. Reflectivity of materials

 R_i represents the reflectivity of differential section i, which is governed by its material properties and incident solar spectrum. It is calculated using the directional hemispherical reflectance $R(\lambda)$ of the material of section i obtained from the Advanced Spaceborne Thermal Emission Reflection Radiometer (ASTER) library, and the hourly clear sky spectral irradiance $G(\lambda)$ generated from the Simple Model of the Atmospheric Radiative Transfer of Sunshine (SMARTS) software [36,40,41]:

$$R_{i} = \frac{\int R(\lambda)G(\lambda) d\lambda}{\int G(\lambda) d\lambda}$$
 (2)

The wavelength range for the integration is from 400 to 4000 nm, covering the typical short-wave radiation range. The yearly spectral irradiance, denoted as $G(\lambda)$, was generated on an hourly basis for the city of Delft. This dataset characterizes the varying solar spectrum profile due to changes in the atmosphere through which the light travels. Consequently, the reflectivity of materials R_i changes with the incident solar spectrum. While the clear sky spectra provide a theoretical maximum under ideal conditions, the employment of the Typical Meteorological Year (TMY) data offers a more realistic solar radiation scenario [42]. Both datasets were temporally aligned, and the hourly spectral profile was adjusted according to the ratio of their respective Global Horizontal Irradiance (GHI) values:

$$G_{adj}(\lambda) = \frac{GHI_{TMY}}{GHI_{SMARTS}}G(\lambda) \tag{3}$$

where GHI_{TMY} is the hourly GHI at Delft from TMY, and GHI_{SMARTS} is the hourly GHI derived by integrating the SMARTS solar spectrum





Fig. 3. The processed ecosystem unit map of the Netherlands (left) compiled for the year 2013, focusing on the city of Delft with the border highlighted in red (right) [39]. Each terrain type is represented by a uniquely colored polygon, encompassing a variety of materials, including water, greenhouse, grassland, residential area, and others. It is important to note that the colors of the polygons are solely for identification purposes and do not correspond to the actual properties of the materials. The albedo simulation is performed over the area highlighted on the right-hand side.

over the specified wavelength range. $G_{adj}(\lambda)$ is the adjusted spectral data used for reflectivity computation.

The material of sections within the studied terrain area was determined using the Ecosystem Unit Map of the Netherlands compiled for the reference year of 2013 [39]. This map captures the different land uses across the country and offers detailed information on the nationwide ecosystem for both natural and man-made areas with precise divisions. Fig. 3 displays this map with a focus on Delft, in which each material type is represented by a uniquely colored polygon for identification. Initially, the map divided the ecosystem into thirty-one key units. Further analysis narrowed down these divisions into ten material classes for the application of this study, which are listed in Table 2. Each material class is represented by a distinct reflectance profile $R(\lambda)$, which corresponds to either one single material or a fusion of multiple materials (Supplementary Table 1). For instance, the road is assigned with the reflectance of pervious concrete, of which over 80 % of the roads in the Netherlands consist [43]. The reflectance profile of coniferous forest predominantly reflects pine trees, whereas deciduous forest equally combines the reflectance values of beech and oak trees [44]. The mixed forest is essentially an equal combination of the coniferous forest and deciduous forest. The reflectance for greenhouses features both the aluminum frame and diffuse glass, where the latter was specifically

Table 2Materials adopted in the GSA model for albedo simulation. The reflectance of SUNPOWER PSR-X21-350 IBC c-Si solar cell is used as the reflectance for PV material.

| Material class | Material reflectance | Seasonal variation |
|----------------------|--|--------------------|
| Water | Water | N |
| Sand | Sand | N |
| Grass/Meadow | Bromus grass | N |
| Road | Pervious concrete | N |
| Coniferous forest | Pine tree | Y |
| Deciduous forest | Beech tree Oak tree Oak bark | Y |
| Mixed forest | Pine tree Beech tree Oak tree Oak bark | Y |
| Residential building | Tiles | N |
| Greenhouse | Diffuse glass aluminum frame | N |
| Industrial building | Asphalt shingle | N |

measured with the PerkinElmer LAMBDA 1050 spectrophotometer for this study [45]. The PV technology selected for this study is interdigitated back contact (IBC) solar cell (SUNPOWER SPR-X21-350 IBC c-Si solar cell), and its spectral reflectance is measured with the same spectrophotometer. This technology is selected because IBC cells have no front-side metal contacts, which eliminates power losses due to metallization shading and aligns best with our scenario where PV is assumed to be fully integrated into building roofs. It is worth noting that this PV technology is adopted for both albedo and rooftop PV simulations. Additionally, the seasonal variation in vegetation was considered, which was reflected by using the ASTER reflectance data of the same material sample measured across different seasons. For example, the reflectance of deciduous forests is the equal combination of beech and oak leaves measured in the corresponding seasons. In winter, the reflectance of oak bark was employed to represent the forest's post-defrost reflectance.

2.1.2. Shading pattern and geometric variables

The shading pattern and the geometric variables, including the view factor F_i and chance factors C_i and C'_i , are derived from LiDAR. LiDAR is a remote sensing technique that is widely used to capture high-resolution topographical information of the Earth's surface. The data is collected by flying a plane equipped with a LiDAR sensor over the target area while sending laser pulses toward the ground. The time required for the reflected signals to return to the sensor provides information about the variation in terrain elevation. In the Netherlands, the LiDAR data is available in several versions and organized into tiles, with each tile covering an area of 6250 by 5000 square meters. The most recent batch of LiDAR data (AHN5) is currently being collected and released. To ensure consistency with the year the Ecosystem map was created, the AHN3 LiDAR dataset is employed, which includes the data collected for Delft in 2014 [46,47]. Working with raw LiDAR data can be time-consuming due to its large amount of data points. To simplify its application, the data is processed using the built-in geoprocessing tool in ArcGIS to generate a Digital Surface Model (DSM). This model is composed of raster data with uniformly sized pixels, where each pixel represents the highest elevation of the data points found within it. In this work, the resolution of the pixel is 1 m, indicating that each pixel corresponds to an area of 1 m². Fig. 4a displays the DSM of a single LiDAR tile, where the height range

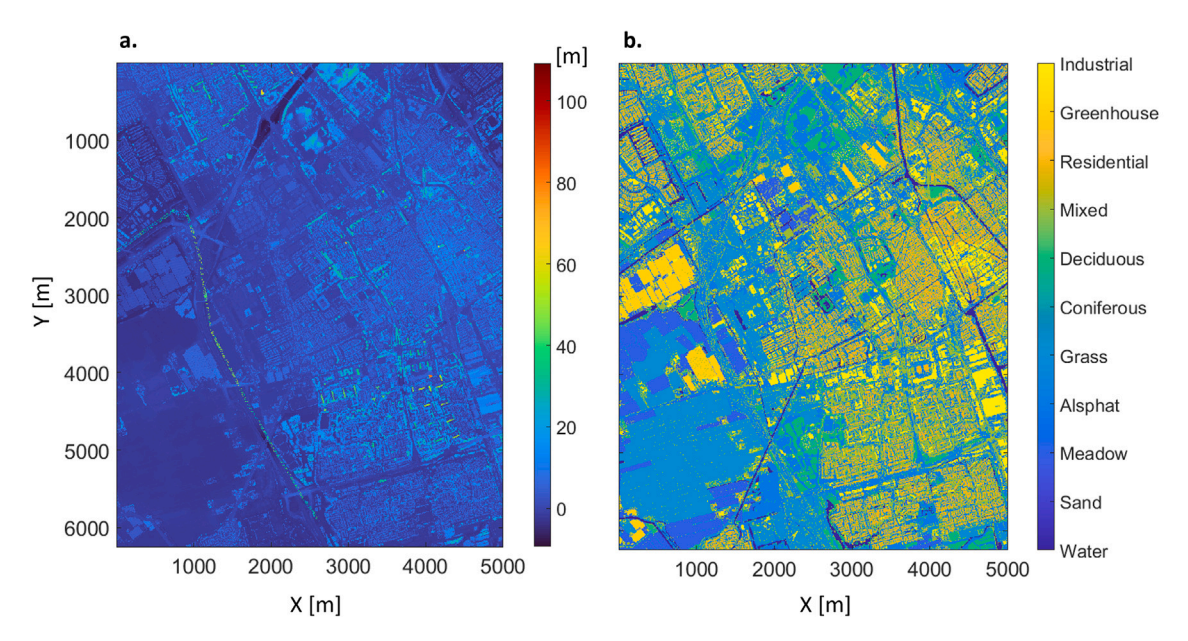


Fig. 4. (a) DSM of one LiDAR tile with an area of 6250 by 5000 square meters. The height values are indicated by the color bar; (b) The same DSM is incorporated with the Ecosystem Unit Map, where each pixel contains both the height and material information.

is indicated by the color bar transitioning from dark blue (lower elevations) to dark red (higher elevations). In Fig. 4b, the Ecosystem Unit Map is merged with the DSM, providing each pixel with detailed information that includes both geographic coordinates and material class.

The DSM is initially employed to generate the hourly shading pattern for albedo calculation. Typically, this shading pattern is derived by performing a line-of-sight (LOS) assessment for each DSM point at various Sun positions, but this method can be computationally heavy and time-consuming due to the large amount of data points to process. To enhance the computational efficiency, an alternative computational geometry operation is used, which involves first transforming the axes of the point cloud to the UQP coordinate system so that the original Z-axis aligns with the Sun's position [48]:

$$\begin{cases} u = x \cos(\psi) - y \sin(\psi) \\ v = x \sin(\psi) + y \cos(\psi) \\ p = v \cos(\theta) + z \sin(\theta) \\ q = -v \sin(\theta) + z \cos(\theta) \end{cases}$$
(4)

In these equations, the x,y, and z are the coordinates of the DSM points, while ψ and θ are the hourly azimuth and altitude of the Sun, respectively. In the UQP coordinate system, the P-axis is aligned parallel to the collimated Sun rays, and the UQ plane is segmented into a regular grid with grid sizes of δ_u and δ_q along U and Q axes, respectively:

$$\begin{cases} i_u = \text{round}(\frac{u}{\delta_u}) \\ i_q = \text{round}(\frac{q}{\delta_a}) \end{cases}$$
 (5)

Given the resolution of the DSM, a grid size of one meter is adopted. Originally, each DSM pixel contains one single height value that represents the highest LiDAR data within the cell. However, the axes transformation rearranges the distribution of DSM points so that multiple points occupy a single grid cell in the UQP coordinate system. Within each cell, the points that are located in the uppermost segment are identified as illuminated. When the Sun's altitude is low, Eq. (4) demonstrates that the transformation becomes significant, leading to a substantial increase in the distance between the points within the

UQP coordinate system. Therefore, after further considering the relatively low point density of the DSM used in this work, the depth of the uppermost segment, d_t , is determined by:

$$d_t = \frac{\text{grid size}}{\sin(\theta)} \tag{6}$$

This threshold ensures the accurate clustering of points into the uppermost segment when the Sun's altitude is low. A detailed visual illustration of this transformation process is provided in the work of A.V. Vo et al. [48]. Fig. 5 displays the hourly shading pattern of one building in Delft using the geometry operation method, with the direction of due North marked on the DSM. The shading results are presented in a binary format, where the illuminated pixels A1 are shown in white, while the shaded pixels A2 are shown in black. As the day progresses, the number of shaded pixels decreases in response to the rising altitude of the Sun. Meanwhile, the orientation of the shading pattern shifts from facing west to east, aligning with the Sun's trajectory from east to west, which clearly demonstrates the evolvement of the shading pattern due to the Sun's movement.

The view factor F_i is calculated through the adapted direct integration method, assuming that the ground is parallel to the hypothetical albedometer S, the area of albedometer S is infinitesimally small, and the area of ground differential section is unit square meter [49]:

$$F_i = \sum_{i=1}^N \frac{\cos \theta_i^2}{\pi d_i^2} \tag{7}$$

where d_i is the linear distance between the albedometer S and the center of ground section i, while θ_i is the angle between this line and the surface normal of ground section i. Here, the hypothetical albedometer S is positioned at the center of the DSM tile, elevated 500 m above the tile's average height. This positioning ensures that the view factors from the entire tile converge at the albedometer [50]. The chance factors C_i and C_i' model the self-shadowing of the surface caused by its roughness. These two probabilities are dependent on the roughness r, which is calculated as the root mean square (RMS) slope of the profile [51]:

$$\sqrt{\frac{(\Delta q_x^2 + \Delta q_y^2)}{2}} \tag{8}$$

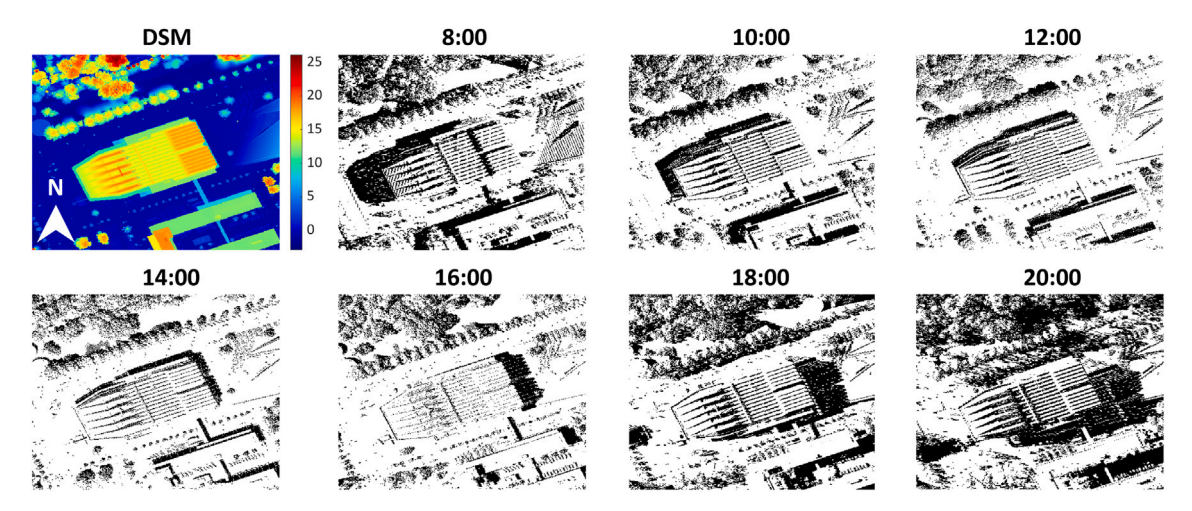


Fig. 5. Hourly shading pattern of one building on the campus of Delft University of Technology (TUD) on the 31st of May, where the direction of due North is marked on the DSM. The shading pattern evolution demonstrates how the shading pattern changes as the day progresses by using the geometry operation method.

where

$$\Delta q_x = \sqrt{\frac{1}{N-1} \sum_{i=1}^{N} \left| \delta_{xi} - \bar{\delta_x} \right|}$$
 (9a)

$$\Delta q_y = \sqrt{\frac{1}{N-1} \sum_{j=1}^{N} \left| \delta_{yj} - \tilde{\delta_y} \right|}$$
 (9b)

The variables δ_{xi} and δ_{yj} are the slopes along x and y directions, respectively, while $\bar{\delta_x}$ and $\bar{\delta_y}$ represent the mean values of these slopes. The chance factors are specifically applied to the illuminated region A1, identifying which sections are self-shadowed or illuminated while remaining visible to the albedometer S. As elaborated in Eq. (1), the view factor of these self-shadowed sections $C_i'F_{S\to A_{i1}}$ is incorporated into the shaded region to complete the albedo computation.

2.1.3. Shade brightness h and irradiance-weighted albedo The variable H is determined by the meteorological data:

$$H = \frac{DNI_M}{DHI_M}\cos\theta_M\tag{10}$$

where θ_M is the angle between the incident irradiance and the normal direction of the differential section. The term 1/(H+1) in Eq. (1) is defined as the shade brightness, which indicates that the albedo increases under overcast sky conditions and at lower solar zenith angles. These predictions are in agreement with the previously published experimental results [52]. Furthermore, the hourly albedo results are weighted based on the irradiance GHI, and the annual average albedo at the location of interest is abtained.

$$\alpha_{weighted} = \frac{\sum_{t=1}^{8760} \alpha_t GHI_{TMY}(t)}{\sum_{t=1}^{8760} GHI_{TMY}(t)} \tag{11}$$

Incorporating GHI into albedo calculation provides a more accurate representation of albedo's impact on the energy balance. This is because the albedo on a sunny day with great GHI contributes significantly more to the Earth's energy balance than the albedo on an overcast day when the GHI is substantially lower. The albedo simulation is conducted on the four tiles covering the DSM of city of Delft, each segmented into a 10 by 13 grid with grid points spaced 500 m apart along both the x and y directions, as shown on the left in Fig. 6. This resolution is chosen to be the same as the one provided in the MODIS products for crossvalidation. To ensure that the view factor converges to one given the height of the hypothetical albedometer S, the DSM from adjacent tiles

is incorporated into the albedo computation. This is illustrated on the right in Fig. 6, where the top left grid point of the tile under simulation integrates missing DSM data from the neighboring tile highlighted in green strips.

2.2. Rooftop PV yield calculation

The framework for rooftop PV calculation was developed based on the simplified skyline-based method [53]. This method estimates the annual energy yield of the rooftop PV installation by correlating the energy production to the sky view factor (SVF) and the Sun coverage factor (SCF) through a polynomial equation:

$$E_Y = \sum_{k=1}^{3} d_k (1 - SCF^k) + (d_4 + d_5 \alpha_{gnd}) SVF$$
 (12)

The SVF represents the fraction of the sky that is visible from a certain point, and the SCF at a location is defined as the ratio between the total annual duration that the Sun is obscured by the PV panel and the skyline to the total sunshine duration at the same location with a clear horizon. The coefficients d_1 to d_5 are obtained from linear and cubic fittings for different combinations of PV tilt and orientation, and α_{gnd} is the ground albedo.

To implement this method, building footprints are first used to identify buildings and extract DSM points for roof surfaces [54]. The extracted roof points are then clustered, and a plane-fitting algorithm is employed on the clustered roof points to determine their orientation and tilt angles [55]. This roof property information is crucial for selecting the appropriate coefficients for energy yield calculation. After that, the skyline profile for each building point is generated by scanning the surrounding environment with a radius of 100 m, and the generated skyline profile serves as the input to compute the SVF and SCF [56]. This process is repeated for all the detected roof points, with Eq. (12) applied to calculate the annual PV electricity production. Here, a PV panel based on IBC c-Si solar cells (SUNPOWER SPR-X21-350) is selected as the PV technology for roof-integrated PV electricity simulation, and two PV integration scenarios are investigated: (1) a scenario where all roof surfaces are assumed to be integrated with PV; (2) a scenario in which only those roof surfaces meeting a specific yield threshold of 650 kWh/kW_p are integrated with PV [57].

2.3. Radiative forcing calculation

The RF calculation is divided into two parts: the positive RF due to albedo decrease and the negative RF resulting from the $\rm CO_2$ concentration reduction in the atmosphere due to the replacement of

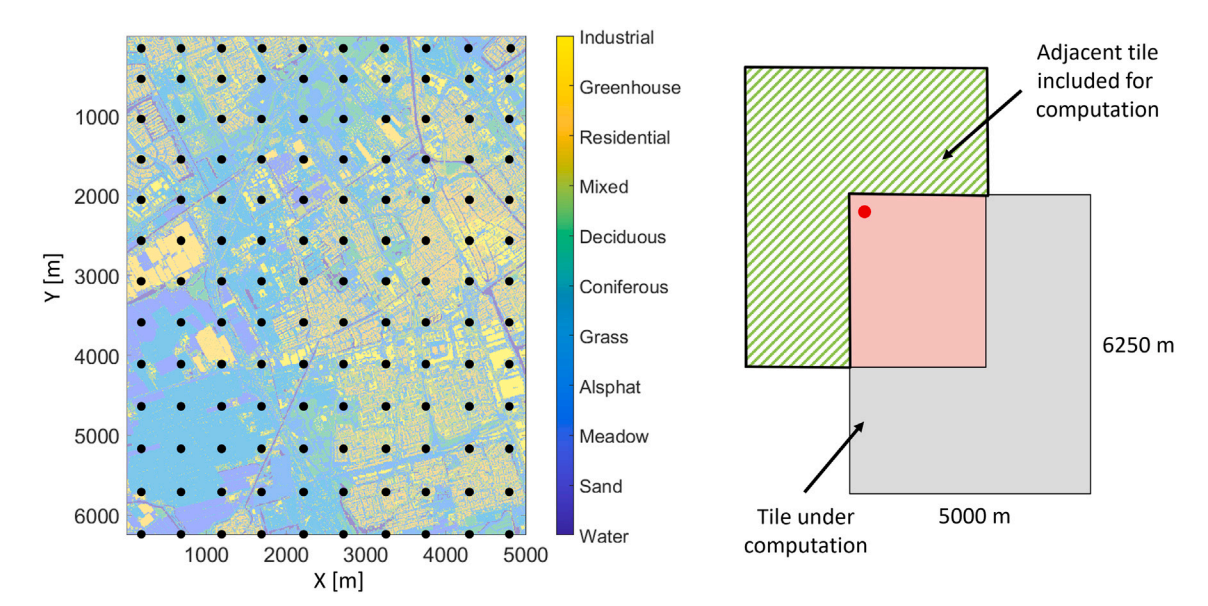


Fig. 6. The albedo simulation is performed on a 10 by 13 grid, with each grid point spaced 500 m apart in both the x and y directions. To ensure that the view factor converges to one, the DSM from the adjacent tile is used, as illustrated on the right.

fossil fuels with PV. The calculations are performed using the albedo simulation results from this work and the inputs published in the paper by Wohlfahrt et al. [58].

The positive RF due to the decrease in albedo is calculated as:

$$RF_{p} = \frac{\sum_{m=1}^{12} K_{m} \Delta \alpha_{m}}{12} \frac{A_{PV}}{A_{E}}$$
 (13)

Here, K_m [W/ m^2] represents the radiative kernel for monthly climatological albedo changes over a decade (2007–2016), which estimates the change in top-of-the-atmosphere (TOA) RF resulting from unit change in albedo [59,60]. In this work, the coordinates of the DSM pixels covering the Delft area are used to retrieve the corresponding radiative kernel values (see Supplementary Tables 2 and 3). $\Delta \alpha_m$ is the albedo change resulting from integrating PV on building roofs, A_{PV} [km 2] is the area of the map pixel influenced by rooftop integrated PV, and A_E [km 2] is the surface area of the Earth. K_m is retrieved for each grid point based on its converted latitude and longitude coordinates, and the positive RF is calculated with its corresponding albedo change [61]. The total positive RF is determined by summing up the RFs of all the grid points.

The negative RF from replacing the fossil fuels with PV is calculated on a monthly basis by converting the generated PV electricity to the equivalent CO₂ reduction:

$$RF_n(t) = k_{CO_2} \int_{t'=0}^{t'=t} I_{carbon} E_{CO_2}(t') IRF_{CO_2}(t-t') dt'$$
 (14)

where k_{CO_2} [1.76×10⁻¹⁵W/m²/kg] is the radiative forcing induced by increasing unit kilogram of CO₂ at a given CO₂ background concentration [62], I_{carbon} [kgCO₂/kWh] is the electricity carbon intensity where the average (2010–2017) value for the Netherlands is used in this work [63], E_{CO_2} [kWh/year] is the annual roof PV electricity generation, IRF_{CO₂} is the impulse-response function modeling the exponentially decaying CO₂ concentration over time after a pulse emission of CO₂ into the atmosphere [64], and t and t' represent the actual and integration time steps, respectively. Based on Eqs. (13) and 14, the equilibrium time ET is calculated at which the negative $RF_p(ET)$ exceeds the positive RF_p .

2.4. MODIS albedo products

The MODIS MCD43A3.h18v03.061 Terra + Aqua BRDF albedo products are downloaded with a spatial resolution of 500 m [65]. Such data

comprise daily albedo records and are requested for a time period of 10 years (2012–2021). Pixels that contain Delft are identified based on their geographical coordinates, ranging from pixel (636,1913) to pixel (655,1928) along longitude and latitude, respectively. After that, the daily white-sky albedo α_{ws} (Albedo_WSA_shortwave) and black-sky albedo α_{bs} (Albedo_BSA_shortwave) are retrieved for the shortwave band for each identified pixel, and further averaged across the chosen decade. The actual daily blue-sky albedo (α_{bs}) is calculated as:

$$\alpha_{bs} = \alpha_{ws} f_{dif} + \alpha_{bs} (1 - f_{dif}) \tag{15}$$

Here, f_{dif} is the annual average of the hourly fraction of global horizontal irradiance relative to the extraterrestrial irradiance.

3. Results and discussion

3.1. GSA albedo results and validation

To analyze the hourly variation in albedo values, the albedo $\alpha_{t,6,5}$ (at grid point located in the 6th row and the 5th column with respect to the top-left corner) is examined. Fig. 7 shows its hourly albedo results and the corresponding GSA variables on both sunny (July 28th) and overcast (July 29th) days. The plots are arranged from top to bottom, where the x-axis indicates the time of the day and the y-axis presents the hourly albedo α , reflectivity R, shade brightness 1/(H+1), view factor of the illuminated and visible sections $F_{S \to A1}$, and the view factor of the shaded and visible sections $F_{S \to A2}$, respectively.

On sunny days with clear skies, albedo is higher at sunrise and sunset hours, while it remains lower for the rest of the day. This diurnal variation in albedo is largely due to the change in the Sun's altitude [66]. At sunrise and sunset, when the Sun is low on the horizon, the sunlight is more likely to be reflected directly back into the atmosphere without interacting with lower objects. As the Sun rises, more sunlight is intercepted by the objects, effectively trapping more radiation within the urban context and consequently lowering the albedo. This behavior is also reflected in the shade brightness, which is higher at sunrise and sunset due to lower DNI. As the day approaches noon, shades are usually darker because of the larger DNI resulting from the higher Sun's altitude. Meanwhile, the change in the Sun's position also affects the distribution of view factors contributed by the shaded and illuminated sections. Higher Sun's altitude leads to more illuminated sections, as illustrated in Fig. 5, which increases the view factor of illuminated and

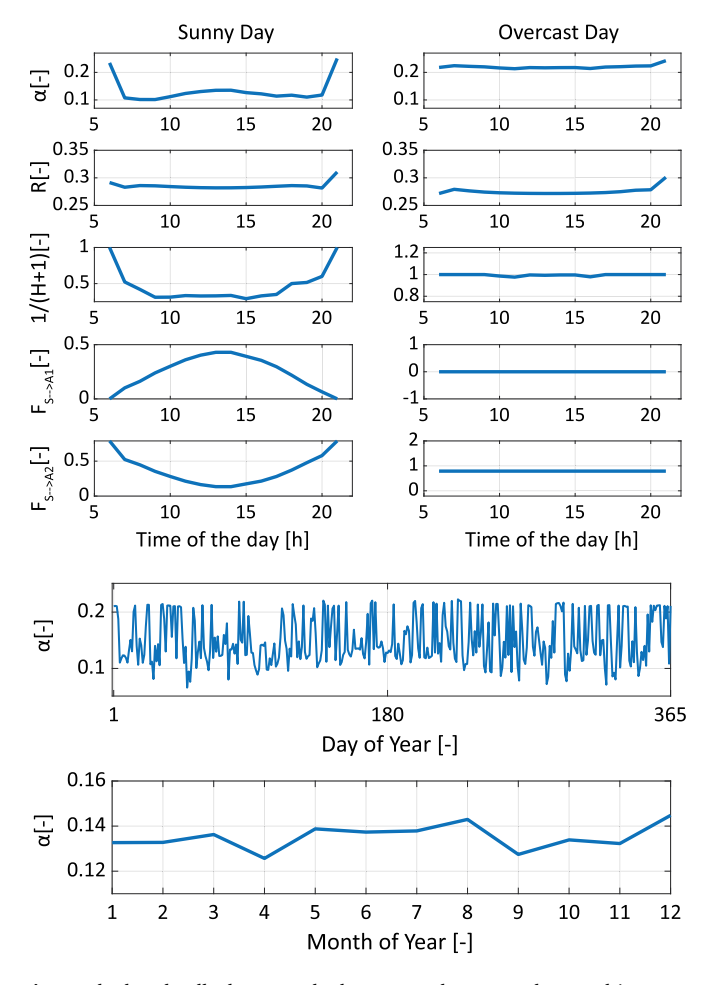


Fig. 7. The hourly albedo $\alpha_{6.5}$ on both sunny and overcast days, and its corresponding GSA variables including reflectivity R, shade brightness 1/(H+1), view factor of the illuminated and visible sections $F_{S\to A1}$, and the view factor of the shaded and visible sections $F_{S\to A2}$. The reflectivity R sets the upper limit of the albedo, and both the shade brightness 1/(H+1) and the view factors $F_{S\to A1,A2}$ determine the variation of the albedo. The daily albedo varies significantly due to the daily fluctuation of meteorological conditions, while the monthly albedo is more consistent throughout the year.

visible sections $F_{S \to A1}$ and reduces the view factor of shaded and visible sections $F_{S \to A2}$. On overcast days, albedo remains high and fairly constant for the entire day. Shade brightness is nearly one, indicating minimal or negligible DNI throughout the day. As a result, the view factor for illuminated and visible sections $F_{S \to A1}$ reduces to zero, whereas the view factor for shaded and visible sections $F_{S \to A2}$ becomes predominant. These daily albedo variation patterns are in line with the albedo measurements on clear and overcast days reported in the literature [38]. Additionally, it can be observed that the reflectivity R is consistently higher than the albedo α for both sunny and overcast days. This means that the reflectivity R sets the upper limit of the albedo, and both the shade brightness 1/(H+1) and the view factors $F_{S \to A1,A2}$ determine the variation of the albedo.

In Fig. 7, the daily and monthly variations in albedo are also presented, with values weighted according to Eq. (11) based on hourly GHI. The daily albedo shows significant fluctuations throughout the year, primarily due to the frequently varying meteorological conditions, as they determine the shade brightness that affects the albedo variation. The monthly albedo exhibits a more regular trend where the weighted albedo stays between 0.12 and 0.15. Typically, the albedo is higher in winter months while lower in summer months, depending on the location

[67]. The integration of GHI into albedo calculation compensates for the monthly variation of GHI, resulting in a more constant albedo value throughout the year. The annual GHI-weighted albedo for this specific grid point $\alpha_{weighted,6,5}$ is calculated to be 0.1352.

The same process was extended to the rest of the grid points, and the annual GHI-weighted albedos derived from the GSA model are shown in Fig. 8a (see Supplementary Table 4 a for numerical results). It can be observed that the albedo values for this area vary from 0.09 to 0.23, with lower values found in urban areas and higher values in surrounding rural areas. This variation can be mainly attributed to the differences in material reflectivity and terrain roughness under identical meteorological conditions. As depicted in Fig. 8c, urban areas typically have lower reflectivity due to the use of absorptive construction materials, which directly contribute to a lower albedo. Meanwhile, as illustrated in Fig. 8d, the urban environments exhibit higher terrain roughness due to densely built constructions and artificial structures, whereas rural areas show significantly lower roughness. This increased terrain roughness in urban areas effectively traps more radiation, reducing the amount that is reflected back into space and consequently lowering the albedo. To evaluate the sensitivity of the GSA albedo to key surface parameters, a local sensitivity analysis is performed by systematically perturbing all surface material reflectivity. PV reflectivity, and terrain roughness by ±20 %. The results, presented in Fig. 9 (see Supplementary Table 5 for numerical results), reveal that increases in all material reflectivity lead to a notable increase in albedo, with a linear response slope of 0.135. Perturbation in PV reflectivity poses only a minor effect (slope = 0.004), mainly because of the small fraction of the roof area replaced by PV material. Conversely, increasing terrain roughness leads to a decrease in albedo, with a negative slope of -0.047. These findings highlight the importance of both material properties and surface complexity in determining albedo, as well as the role of dense urban morphology in trapping solar radiation and reducing reflected energy. Considering the strong linear correlation between surface material reflectivity and albedo results, the uncertainty introduced by non-representative material selection or assignment is likely the major source of error in the GSA albedo model.

Fig. 8b shows the MODIS albedo results over the same area, which are obtained by averaging daily albedo values over a decade (2012–2021). While the MODIS albedo map presents a similar distribution pattern to the one derived from the GSA model, with lower albedo values in urban areas and higher values in surrounding rural areas, there are some differences: first, the urban area characterized by lower albedo appears smaller in the GSA albedo map; second, the albedo values in the surrounding rural areas are higher in the GSA albedo map. Considering the sources of uncertainty from the GSA albedo model, these discrepancies can be mainly attributed to the incompleteness of the material reflectivities employed in the simulations. As depicted in Fig. 8e, the differences in albedo are concentrated largely in rural regions and parts of the urban area, which closely match the reflectivity map. This suggests that variations between GSA and MODIS albedo maps are mainly driven by the choice of material reflectivities. Here, ten representative material classes are implemented for the albedo simulation. However, in reality, the materials are highly diverse and can vary depending on the location, regulations, and specific requirements. Completing the material database and refining material assignments in the DSM could enhance the accuracy of simulated albedo results. Additionally, the method used to generate the hourly shading profile can also affect albedo outcomes. While the employed geometry operation is time efficient, it offers lower accuracy compared to the LOS method considering the resolution of the DSM. This may result in inaccuracies in the shading profile, where some pixels that should be shaded are incorrectly classified as illuminated, and vice versa. Meanwhile, the simulated albedo values represent the case with the albedometer positioned at 500 m above the ground. Converting these values to TOA albedo requires an additional correction for atmospheric attenuation, which typically reduces the albedo values.

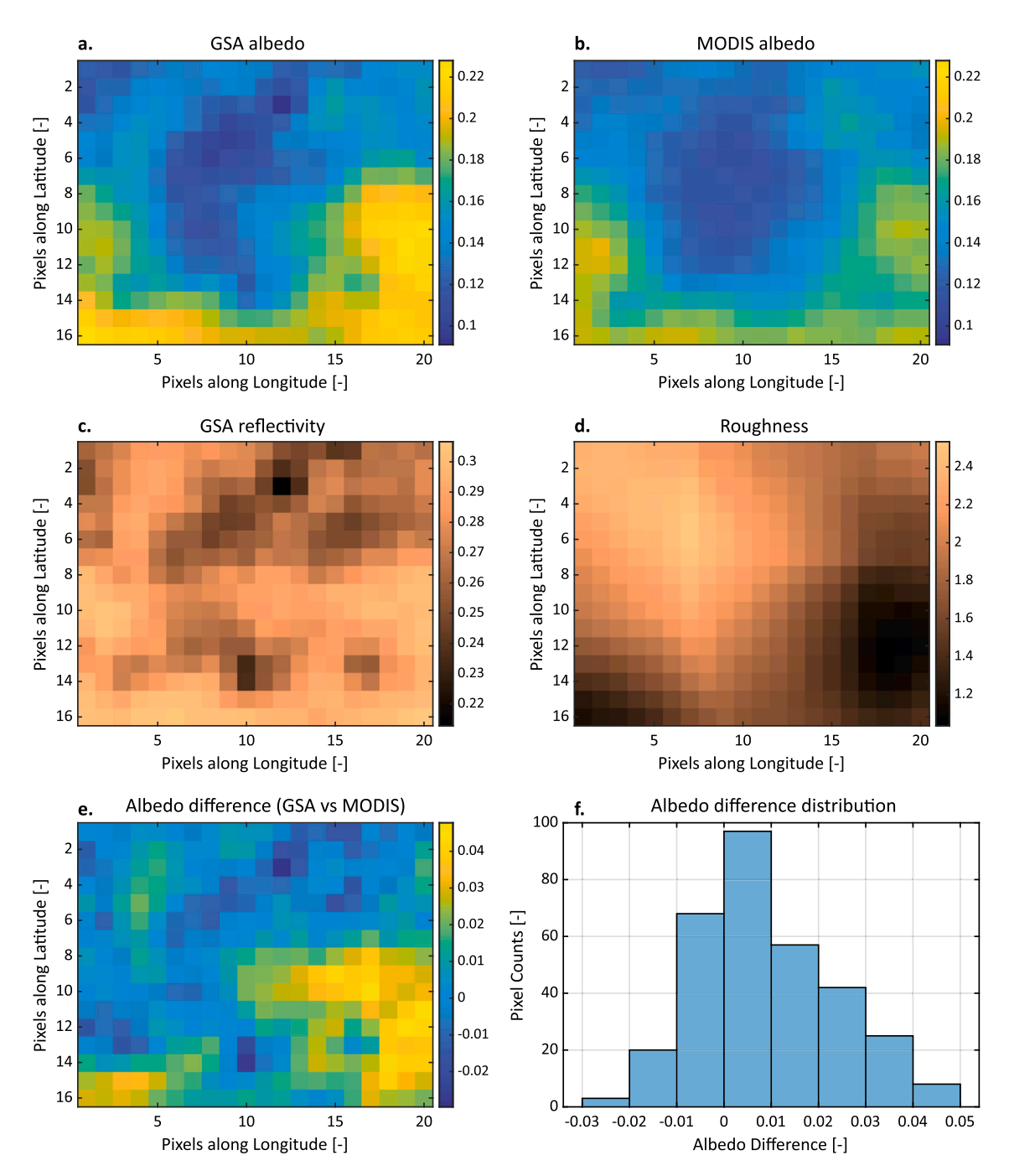


Fig. 8. The albedo map of the rectangular area covering Delft, including (a) The GHI-weighted annual average albedo from the GSA model; (b) The blue-sky albedo from MODIS averaged over year 2012 to 2021; (c) The annual average reflectivity from the GSA model; (d) The roughness from the GSA model; e) The albedo difference between the GSA model and MODIS products; (f) The distribution of the albedo differences.

Considering the sources of uncertainty in the MODIS albedo product, the albedo difference can be introduced from several factors: the quality of measurement data, the assumptions and limitations of the bidirectional reflectance distribution function (BRDF) model used to derive albedo, and the biased measurement data due to complex geometry and anisotropic surfaces in the urban environment. First, MODIS sensors collect directional reflectance of surfaces from different viewing angles. The successful observation, however, is subject to cloud-free conditions. If multiple observations over the 16-day window are cloud-contaminated, the BRDF model cannot be reliably fitted, resulting in invalid or low-quality albedo values. Filtering out these invalid albedo

values can lead to a less representative yearly average albedo. Second, the BRDF model implemented to compute MODIS albedo is a semi-empirical model originally developed for homogeneous and temporally stable surfaces. Therefore, it is more suitable for vegetated surfaces whose conditions do not change significantly during satellite observation, and it is less suited for complex urban environments or for dynamic surfaces featuring vegetation growth cycles [68,69]. Third, urban areas are characterized by high spatial heterogeneity and fast-varying geometry. Within a single MODIS pixel, rooftops, roads, vegetation, or any type of urban artifacts may all contribute to the observed signal. This means that different materials can dominate the reflectance signal at different

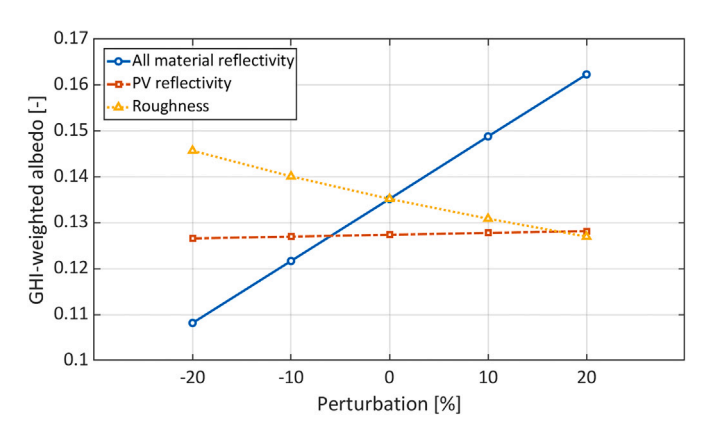


Fig. 9. Sensitivity analysis of the GSA albedo model on $\alpha_{weighted,6,5}$ with respect to material reflectivity, PV reflectivity, and surface roughness perturbations.

times when the pixel is observed from changing viewing angles within the 16-day window. This angular inconsistency in reflectance sampling can introduce deviations in the derived albedo [70].

Fig. 8f presents a histogram plot that clusters the albedo differences into eight bins. According to this analysis, 71.56 % of the pixels in the GSA albedo map have higher albedo values compared to the MODIS albedo map. More specifically, 51.56 % of the pixels differ by ± 0.01 , 75.62 % of the pixels differ by ± 0.02 , and 89.69 % of the pixels differ by ± 0.03 . The overall average albedo of the entire area is found to be 0.1584 for the GSA model and 0.1493 for MODIS products, leading to an absolute error of 6.12 %.

3.2. Annual roof PV energy from simplified skyline-based method

Fig. 10a shows the annual PV energy yield map for the first scenario, in which all roof surfaces are assumed to be integrated with PV. The x- and y-axes represent the absolute distances of the area along longitude and latitude in meters, respectively, with due North indicated in the bottom left corner of the figure. The energy yield per square meter is depicted by a color scale, transitioning from black (low yield) to white (high yield). It can be observed that in the densely constructed urban area, the PV potential is relatively lower due to the elevated skyline.

The north-facing roof surfaces also provide lower PV potential due to the suboptimal orientation. Fig. 10b presents the results for the second scenario, where only the roof surfaces meeting the specific yield threshold of 650 kWh/kW $_p$ are integrated with PV. This leads to fewer roof pixels on the solar map, primarily those within urban areas or with unfavorable orientations, as they often fail to meet the required specific yield threshold. As a result, the total PV integrated roof area is decreased from 2.8289 km 2 to 2.2425 km 2 . The total annual roof-integrated PV yield for Delft is further calculated to be 485.72 GWh/year and 434.82 GWh/year for the first and second scenarios, respectively.

3.3. Positive and negative radiative forcings

The positive RF is calculated from the decrease in albedo after the integration of PV on building roof surfaces. Fig. 11a shows the albedo map of the same rectangular area covering Delft after all the roof surfaces are replaced with PV (see Supplementary Table 4 b for numerical results). Compared to Fig. 8a, this map presents a noticeable reduction in albedo within the urban area. Fig. 11b displays the location and extent of the albedo decrease, with a color bar transitioning from black (indicating a large decrease) to white (indicating a small decrease). The maximum absolute albedo reduction due to roof PV integration is found to be -0.0306. From Eq. (13), the positive RF after integrating PV into all detected roof surfaces in Delft is calculated to be 3.53×10^{-8} W/m². Assuming a grid carbon emission intensity of 437 g CO2-eq/kWh, the negative RF is calculated from Eq. (14), and the equilibrium time is determined to be 39.2 days [63]. The same process is repeated for scenario two (see Supplementary Table 4 c for numerical results), and the positive RF and the equilibrium time are found to be $3.40\times10^{-8}\ \text{W/m}^2$ and 42.0 days, respectively. For both scenarios, the negative RF from PVgenerated electricity offsets the positive RF from albedo reduction in around forty days. This rapid offset can be mainly attributed to the fact that the urban environment already has a low albedo, which minimizes the impact of the further albedo reductions on positive RF caused by PV integration. Conversely, integrating PV in areas with high initial albedo would result in a more substantial decrease in albedo, thereby extending the time required to offset the associated positive RF. Meanwhile, PV has a relatively high energy density (171.1 kWh/m² for scenario one and 193.9 kWh/m2 for scenario two), leading to a larger negative RF per unit area of PV integration. Even when PVs are integrated on roofs with unfavorable orientations, their high energy density is sufficient to

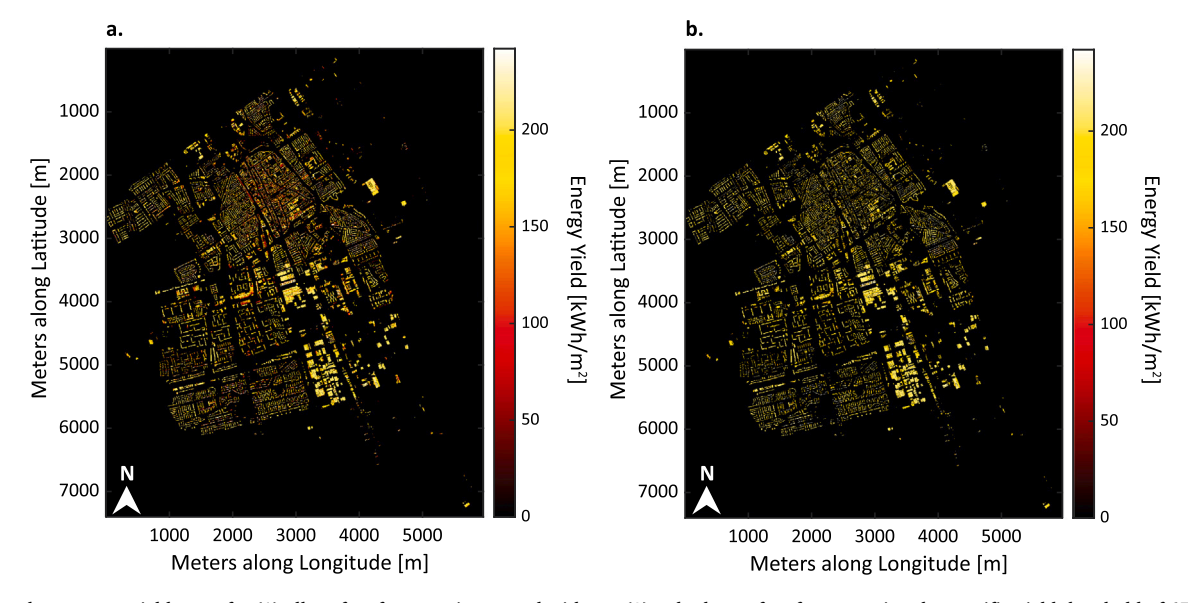
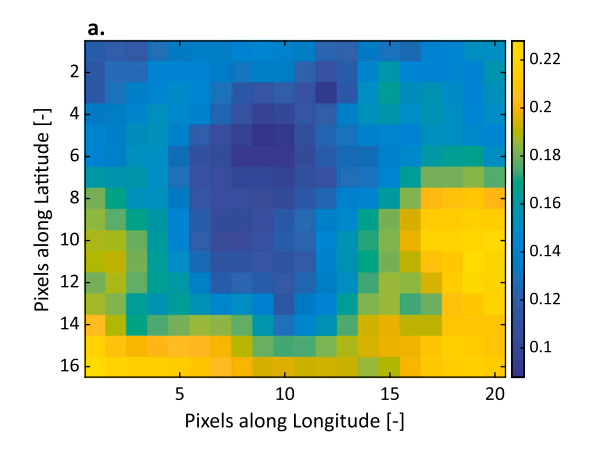


Fig. 10. Annual PV energy yield maps for (1) all roof surfaces are integrated with PV; (2) only the roof surfaces meeting the specific yield threshold of 650 kWh/kW $_p$ are integrated with PV.



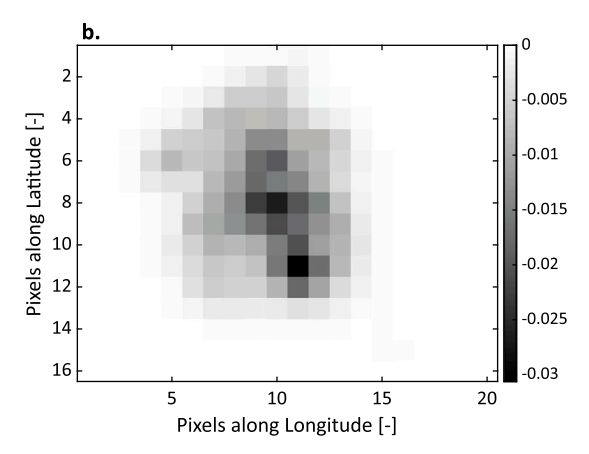


Fig. 11. (a) The albedo map of the rectangular area including Delft after replacing all the roof surfaces with PV; (b) The absolute albedo difference on the map before and after PV integration on all the roof surfaces in Delft.

Table 3The cumulative negative RF from roof PV integration in Delft over 5, 10, 15, 20, 25, and 30 years.

| Cumulative years | Scenario 1 (\times 10 ⁻⁶ W/m ²) | Scenario 2 (\times 10 ⁻⁶ W/m ²) |
|------------------|---|---|
| 5 | 1.70 | 1.52 |
| 10 | 3.10 | 2.77 |
| 15 | 4.40 | 3.94 |
| 20 | 5.61 | 5.02 |
| 25 | 6.74 | 6.03 |
| 30 | 7.85 | 7.03 |

offset the positive RF induced by albedo changes at a relatively fast pace, which leads to a slightly extended equilibrium time in scenario two.

Once the PV system is in operation, it continues to contribute to negative RF throughout its lifetime as long as the energy system is not fully decarbonized. Table 3 presents the cumulative negative RF from roof PV integration in Delft over 5, 10, 15, 20, 25, and 30 years. The results assume a constant annual PV electricity yield and a fixed grid carbon emission intensity. As expected, the cumulative negative RF increases over time, while the increment between every 5-year interval gradually decreases. By the end of the PV system's typical lifetime (between 25 and 30 years), the cumulative negative RF reaches 6.74 and 7.85×10^{-6} W/m² for scenario one and 6.03 and 7.03×10^{-6} W/m² for scenario two. These numbers are approximately 170 to 230 times larger than the initial positive RF caused by albedo reduction. However, it is worth noting that PV electricity production declines over time in practice due to module degradation, and the carbon emission intensity of the grid is expected to decrease as energy systems decarbonize. Therefore, these values may be overestimated.

Globally, albedo typically increases with latitude, being higher at higher latitudes and vice versa [71]. PV generation profile, in contrast, is the opposite, where PV yield peaks at lower latitudes and decreases towards higher latitudes. Therefore, integrating PV at higher latitudes would result in a longer timespan to offset the positive RF due to relatively larger albedo reduction and smaller PV generation. Regionally across Europe, surface albedo varies due to differences in land cover and seasonal conditions. In northern Europe, albedo tends to be higher, especially in winter with widespread snow cover. Moving southward into central Europe, the surface albedo generally decreases as the land-scape transitions to a mix of forests, grassland, and urban areas. The Netherlands falls within this lower-to-middle surface albedo range due to its mixed urbanized and agricultural landscapes. In southern Europe, surface albedo increases again due to a more open landscape and less dense vegetation [72]. This spatial distribution indicates that under

original surface albedo conditions, central Europe contributes more to positive RF. Meanwhile, PV deployment in northern and southern Europe leads to larger increases in positive RF because of higher initial albedo values. However, further considering the cloud cover may influence this effect [73]. In regions with frequent cloudy or overcast weather, such as the Netherlands and northern Europe, the positive RF due to albedo change is partially mitigated, as less incoming solar radiation reaches the surface. In contrast, southern Europe typically experiences more clear and sunny weather, leading to stronger positive RF from albedo reduction, but this effect can be offset more quickly by the higher PV yield.

With ongoing advancements in the PV industry, PV cells are designed to be more absorptive, featuring lower reflectivity, yet delivering higher efficiency attributed to the mature manufacturing processes and innovative cell architectures. This reduction in reflectivity leads to a decrease in albedo, thereby increasing the positive RF when PVs are integrated into areas with initially higher albedo. On the other hand, the enhanced efficiency of PV cells converts more solar energy into electricity, which reduces the timespan that is required to offset the positive RF. Therefore, there is a trade-off between reducing reflectivity and increasing efficiency in the RF effects of PV cells. Considering that the reflectivity of PV cells is already very low, the benefits from increased efficiency would outweigh those from reduced reflectivity, meaning that installing highefficiency PV cells in urban areas is more advantageous to the energy balance of the Earth during the transition to a fully renewable-energypowered future. However, from a long-term perspective, once fossil fuels are completely phased out, the reduced albedo from PV installation will still increase the positive RF, regardless of the efficiency of PV cells. This occurs because the electricity generated by PV cells is ultimately converted to heat that is released into the environment. A potential solution is the development of colored PV cells designed to mimic the color and appearance of the background materials or of the infrared filters that reflect the unwanted irradiance back into the space [74]. The former approach preserves original albedo values while generating green electricity. In a strategic scenario, reflectivity could be optimized based on the city-scale PV yield simulations to maximize albedo and still meet the local energy demands. In this way, the overall albedo of urban environments would be increased, minimizing the positive RF and still securing a sustainable supply of green electricity.

4. Limitations and outlook

This section outlines the key limitations encountered during the study and presents future research directions for potential investigation.

4.1. Employ up-to-date input datasets with higher quality

The LiDAR data used in this project were collected in 2014, consistent with the reference year of the Ecosystem Unit Map. As a result, any structural or environmental changes after 2014, such as vegetation growth or urban development, are not captured. This temporal mismatch can introduce discrepancies in the results; outdated material classifications may misrepresent current surface conditions in albedo simulations, and changes in rooftop geometry may make previously available surfaces unsuitable for PV installation. The LiDAR dataset offers a resolution of about 3-5 points per square meter, with over 99.7 % of the points having a vertical accuracy within 20 cm. While this density is decent for a city-scale analysis, it is insufficient to reliably identify smaller and lower-profile rooftop features or sharp building edges, which are critical for accurate PV yield calculations. Meanwhile, the material classification in the Ecosystem Unit Map consists of thirty-one key units, which are further simplified into ten material classes for the application of this study. While this reduction facilitates large-scale albedo analysis, it does not fully reflect the complexity of real-world surface materials. The simplified reflectivity classification can lead to deviations in albedo simulation results. Future studies would benefit from employing more recent and higher-resolution LiDAR data and material maps, along with a more comprehensive and representative material reflectance database to improve model accuracy and relevance.

4.2. Local and regional dynamic albedo monitoring

The GSA albedo simulation framework developed in this study can be extended to monitor dynamic local and regional albedo variations. At the local scale, albedo simulation can support the assessment and prediction of urban heat island effects caused by changes in urban morphology, offering urban planners insights for designing more sustainable and thermally comfortable cities. Additionally, understanding local albedo improves knowledge of surface energy balance, which directly influences soil temperature. This is an essential factor in agriculture and soil carbon storage. As demonstrated in this work, albedo is linked to global warming. Expanding the model to the regional scale can help quantify the contribution of each country to global warming due to morphology-induced albedo reductions. Additionally, regional albedo variations affect global and mesoscale climate patterns, making albedo monitoring valuable for improving meteorological analysis and weather forecasting. To enable these applications, the current albedo model should be adapted to account for both sky view factors and ground view factors considering the influence of surrounding structures. For instance, the local albedo of an open field enclosed by buildings should include the view factors and material reflectances of building facades to deliver accurate and representative albedo simulation results.

4.3. Support current and future life cycle assessment (LCA) of PV technology

The current simulation framework considers exclusively the positive RF associated with albedo reduction due to urban roof PV integration, which is the primary scope of this study. However, it is important to recognize that the full life cycle of PV modules, including solar cell production, module manufacturing, transportation, operation, disposal, and recycling also contributes to CO2 emissions. For c-Si PV modules, the typical carbon emission intensity ranges from 13 to 30 g CO2eq/kWh, which is significantly smaller than that of fossil fuel-based electricity (437 g CO₂-eq/kWh for the Netherlands in 2017) [63,75]. Under the current carbon-intensive energy infrastructure, the equilibrium time remains short as demonstrated, indicating that albedo-related positive RF has a minor role. However, as the energy infrastructure decarbonizes through the penetration of renewable energies, the grid's carbon emission intensity progressively decreases. In a future scenario where electricity supply is predominantly based on renewable energy and the grid's carbon emission intensity decreases to the level associated with current c-Si PV modules, the equilibrium time for a fully integrated roof PV scenario in Delft extends to 1548.5 days and 623.1 days under the 13 g and 30 g $\rm CO_2$ -eq/kWh cases, respectively. As the global energy structure becomes more sustainable and PV's carbon emission intensity continues to decline with technological advancements, the relative impact of albedo-induced positive RF on global warming will become more pronounced. This highlights the importance of incorporating the albedo effects of PV deployment into future LCA to provide a more realistic evaluation of the global warming mitigation potential of PV technology.

4.4. Incorporate cloud dynamics and tilted PV to albedo simulation

In the current simulation framework, the dynamic behavior of moving clouds is not sufficiently accounted for. Overcast conditions are represented by a fully cloudy scenario, where all DSM pixels are assumed to be shaded. However, in reality, cloud coverage sometimes is partial and variable, which casts shadows on only sections of the terrain. This limitation may introduce inaccuracies, particularly during noon hours when solar irradiance is relatively high. Future efforts can be made to incorporate cloud information to refine the hourly shading profiles of each DSM pixel. This could be achieved by either employing sky images that track the movement of clouds or by incorporating a cloud coverage probability factor based on the local meteorological cloud maps. Meanwhile, PV tilt in the current simulation framework is inherited directly from the roof geometry derived from the DSM, meaning that PV panels adopt the existing roof tilt and orientation. In practice, however, PV panels are often installed at certain tilt and orientation on flat roofs to optimize energy throughput. These tilted PV panels have different sky view factors and can exhibit different radiative behaviors compared to flat-mounted PV panels. Future work can explore the influence of tilted PV panels on both albedo and net radiative forcing.

4.5. Improving computational efficiency

As reported in Section 3.1, the average albedo simulation time for one grid point is found to be 1.29 hours based on the computer configuration employed. There are a couple of approaches to optimize the computational efficiency:

- Employing a DSM with a larger cell size: the current study employs a DSM with a cell size of 1 m². Increasing the cell size can reduce the number of points to be simulated, thereby improving the computational efficiency. However, this comes at the cost of reduced spatial resolution, which can compromise the accuracy of surface morphology representation and degrade the simulation results. A sensitivity analysis is necessary to find out the optimal cell size that balances simulation accuracy and computational efficiency. This optimal resolution is expected to be morphology-dependent, where areas with less morphology variation and uniform material composition are likely to be less sensitive to the DSM cell size, while densely urban environments with complex surface features and heterogeneous materials will require higher resolution to maintain accuracy.
- Preprossing input data to avoid repetitive computation: in the current workflow, material assignment to DSM is performed separately for every grid point, which takes on average 8.6 minutes. This repetitive step can be avoided by pre-assigning the material classes to the entire DSM. During albedo simulation, the relevant subset of the DSM can then be extracted based on the area of study. Another time-consuming step is the hourly shading profile generation for each DSM pixel. As these profiles are solely dependent on the Sun's position assuming the cloud coverage is not considered, they can be precomputed and saved. During albedo simulation, the corresponding shading profiles at a given time and location can be retrieved and applied, thereby facilitating the overall simulation process.

5. Conclusions

In this work, a comprehensive methodology was developed to quantify both the positive and negative radiative forcing (RF) effects of distributed urban rooftop PV deployment using a high-resolution approach. Earlier studies often rely on coarse-resolution satellite data, which cannot capture the spatial variance of distributed urban PV systems, or on simplified PV assumptions that may lead to inaccurate estimations of PV yield and albedo change. To address these limitations and to fill this research gap, this study introduced two novel simulation frameworks that leverage LiDAR data and geo-referenced material maps. The first framework, based on geometric spectral albedo (GSA) model, simulates surface albedo change before and after PV deployment. The second framework, utilizing skyline-based PV model, performs large-scale rooftop PV simulation for annual yield calculation. Both frameworks were established to accurately calculate the radiative impacts of urban rooftop PV integration. The outputs were then translated into positive and negative RFs to calculate the equilibrium time the period required for the negative RF from PV electricity generation to fully offset the positive RF from albedo reduction.

The workflow was applied across a rectangular area covering the entire city of Delft. The hourly albedo results showed distinct patterns: on sunny days with clear skies, albedo peaks at sunrise and sunset hours but remains lower for the rest of the day. On overcast days, albedo stays relatively high and constant for the entire day. The annual GHI-weighted albedo was calculated and mapped to the selected area, presenting lower albedo values in urban areas and higher values in surrounding rural areas. This distribution can be attributed to the use of low-reflectivity materials commonly found in urban settings, which directly reduce surface albedo, as well as the greater roughness within urban environments, which traps more radiation and limits the amount of energy reflected back to space. The simulation results were validated with MODIS albedo products, showing a general agreement in albedo distribution patterns despite differences in absolute albedo values. Overall, around 90 % of the map pixels from the GSA model lay in a deviation range of ±0.03 from the MODIS products. The average albedo simulated for the entire area was 0.1584 for the GSA model and 0.1493 for the MODIS product, leading to an absolute difference of 6.12 %. This discrepancy could be attributed to several sources of uncertainty. From the GSA albedo model perspective, the main contributors were the limited assumptions in the classification of surface materials and the simplified geometric operations used to derive the shading profile. On the other hand, uncertainties in the MODIS albedo product came primarily from measurement data quality, the BRDF model that is less suited for spatially heterogeneous and temporally dynamic urban surfaces, and the complex urban geometry that responds to varying surface reflections during the multi-day satellite observation period.

The annual PV energy yield was investigated under two scenarios: 1) all roof surfaces are integrated with PV; 2) only the roof surfaces meeting the specific yield threshold of 650 kWh/kW $_{p}$ are integrated with PV. In the first scenario, the total annual PV yield amounts amounted to 485.72 GWh/year, covering a roof area of 2.8289 km². In the second scenario, where only high-yielding roofs were integrated with PV, the yield was slightly lower at 434.82 GWh/year, with a covered roof area reduced to 2.2425 km². For both scenarios, the positive RFs due to rooftop PV integration are determined at 3.53×10^{-8} W/m² and 3.40×10^{-8} W/m², respectively. Together with the negative RF derived from the PV yield, the equilibrium time (ET) was found to be 39.2 and 42.0 days, assuming a grid carbon intensity emission of 437 g CO2-eq/kWh. This ET is considered as remarkably short for mainly two reasons: first, this duration represents only less than 0.5 % of typical PV module lifetime (25 to 30 years). This means that for over 99.5 % of its operational lifespan, PV technology is contributing to the negative RF as long as it continues to displace fossil-fuel-generated electricity; second, compared to other renewable energies such as hydropower, this duration is significantly shorter. For example, a recent study found out that 43 % of investigated hydropower plants achieve equilibrium within 4 years (around 5 % of their estimated lifetime of 80 years), while 19 % exceed 40 years, and 12 % never reach equilibrium within their operational lifetime [58].

The cumulative negative RF from roof PV integration in Delft by the end of PV system's typical lifetime (between 25 to 30 years) was found to be 6.74 and $7.85 \times 10^{-6} \text{ W/m}^2$ for scenario one and 6.03 and 7.03 $\times\,10^{-6}~\text{W/m}^2$ for scenario two, assuming a fixed carbon emission intensity and annual PV yield. These numbers are approximately 170 to 230 times larger than the initial positive RF caused by albedo reduction. This finding indicates that the reduction in greenhouse gas emissions facilitated by PV integration significantly outweighs the positive RF caused by the reduced albedo under current carbon-intensive energy infrastructure. However, as energy infrastructure continues to decarbonize with the increasing penetration of renewable sources, the carbon emission intensity of the grid declines accordingly. In a future scenario where electricity generation is predominantly based on renewables—and the grid's carbon intensity approaches that of current c-Si PV modules—the equilibrium time for a fully integrated rooftop PV system in Delft extends significantly, reaching 1548.5 days and 623.1 days under the 13 g and 30 g CO₂-eq/kWh scenarios, respectively. As the energy system becomes more sustainable and PV manufacturing emissions continue to decrease through technological advancements, the relative contribution of albedo-induced positive radiative forcing to net climate impact will become increasingly significant. This highlights the necessity to account for albedo effects in future life cycle assessments (LCA) of PV technologies to more accurately evaluate their global warming mitigation

This study can be extended to other regions of the world as long as the digital elevation data and material class data are available. Therefore, this work aids in the high-resolution assessments of global albedo and its variation, and offers insights into the Earth's energy balance by examining both the positive and negative RFs caused by PV integration. These findings contribute to achieving a more realistic figure of climate change mitigation potential through PV technologies.

CRediT authorship contribution statement

Olindo Isabella: Supervision, Writing – review & editing, Funding acquisition. Miro Zeman: Funding acquisition. Hesan Ziar: Writing – review & editing, Resources, Investigation, Conceptualization, Supervision, Methodology, Formal analysis. Shredatta Marathe: Methodology, Formal analysis, Software, Investigation, Data curation. Yilong Zhou: Writing – review & editing, Visualization, Software, Methodology, Formal analysis, Conceptualization, Writing – original draft, Validation, Resources, Investigation, Data curation.

Declaration of competing interest

The authors declare that they have no known competing financial interests or personal relationships that could have appeared to influence the work reported in this paper.

Acknowledgement

This work was supported by the project Future Factory (TEUE919002), which received funding from the Dutch Ministry of Economic Affairs and Climate Policy.

Data availability

This study was carried out using publicly available data, where LiDAR data were obtained from PDOK at https://www.pdok.nl/introductie/-/article/actueel-hoogtebestand-nederland-ahn, the building footprints from PDOK at https://www.pdok.nl/introductie/-/article/basisregistratie-adressen-en-gebouwen-ba-1, the Eco-system Unit Map from CBS at https://www.cbs.nl/en-gb/background/2017/12/ecosystem-unit-map, the SMARTS data from NREL at https://www.nrel.gov/grid/solar-resource/smarts.html, the ASTER spectral reflectance data at ECOSTRESS spectral library (formerly

ASTER spectral library) from https://speclib.jpl.nasa.gov/download, and the albedo change radiative kernel at EDI data portal from https://portal.edirepository.org/nis/mapbrowse?packageid = edi.396.1.

The MATLAB code and research data are freely available at https://doi.org/10.4121/136d3808-cb58-4276-8d5b-4a4e2cd5e38c.v1.

Appendix A. Supplementary data

Supplementary data to this article can be found online at doi:10. 1016/j.apenergy.2025.126544.

References

- Key aspects of the paris agreement | UNFCCC. [Online]. Available: https://unfccc. int/most-requested/key-aspects-of-the-paris-agreement
- [2] Millar RJ, Fuglestvedt JS, Friedlingstein P, Rogelj J, Grubb MJ, Matthews HD, et al. Emission budgets and pathways consistent with limiting warming to 1.5 °C. Nat Geosci 2017; 10(10):741–7.
- [3] Record-breaking annual growth in renewable power capacity. [Online]. Available: https://www.irena.org/News/pressreleases/2025/Mar/Record-Breaking-Annual-Growth-in-Renewable-Power-Capacity
- [4] Ember. Share of electricity generation from solar energy worldwide from 2010 to 2023 [Graph]; 2024. [Online]. Available: https://www.statista.com/statistics/ 1302055/global-solar-energy-share-electricity-mix/
- [5] Enabling framework for renewables. [Online]. Available: https://energy.ec.europa.eu/topics/renewable-energy/enabling-framework-renewables_en
- [6] Top countries in the race to net zero emissions | Net0. [Online]. Available: https://net0.com/blog/net-zero-countries
- [7] Haegel NM, Verlinden P, Victoria M, Altermatt P, Atwater H, Barnes T, et al. Photovoltaics at multi-terawatt scale: waiting is not an option. Science 2023; 380(6640):39–42.
- [8] Parker J. The Leeds urban heat island and its implications for energy use and thermal comfort. Energy Build 2021; 235:110636.
- [9] Fakhraian E, Alier M, Dalmau FV, Nameni A, Guerrero JC. The urban rooftop photovoltaic potential determination. Sustainability 2021; 13(13):7447.
- [10] Zhou Y, Verkou M, Zeman M, Ziar H, Isabella O. A comprehensive workflow for high resolution 3D solar photovoltaic potential mapping in dense urban environment: a case study on campus of Delft University of technology. Sol RRL 2021; 6(5):2100478.
- [11] Chen H, Chen W. Status, trend, economic and environmental impacts of household solar photovoltaic development in China: modelling from subnational perspective. Appl Energy 2021; 303:117616.
- [12] Zhang Z. Chen M., Zhong T., Zhu R., Qian Z., Zhang F., Yang Y., Zhang K., Santi P., Wang K., Pu Y., Tian L., Lü G., and JYan J., Carbon mitigation potential afforded by rooftop photovoltaic in China. Nat Commun 2023; 14(1):1–12.
- [13] Tsoutsos T, Frantzeskaki N, Gekas V. Environmental impacts from the solar energy technologies. Energy Policy 2005; 33(3):289–96.
- [14] Genchi Y, Ishisaki M, Ohashi Y, Kikegawa Y, Takahashi H, Inaba A. Impacts of large-scale photovoltaic panel installation on the heat island effect in Tokyo. in: Fifth Conference on the Urban Climate; 2003.
- [15] Taha H, Akbari H, Rosenfeld A, Huang J. Residential cooling loads and the urban heat island—the effects of albedo. Build Environ 1988; 23: 271–83.
- [16] Taha H. The potential for air-temperature impact from large-scale deployment of solar photovoltaic arrays in urban areas, Sol Energy 2013; 91: 358–67.
- [17] Sailor DJ, Anand J, King RR. Photovoltaics in the built environment: a critical review. Energy Build 2021; 253:111479.
- [18] Zhong Y, Yu H, Wang W, Yu P. Impacts of future urbanization and rooftop photovoltaics on the surface meteorology and energy balance of Lhasa, China. Urban Clim 2023: 51:101668.
- [19] Masson V, Bonhomme M, Salagnac JL, Briottet X, Lemonsu A. Solar panels reduce both global warming and urban heat island. Front Environ Sci 2014; 2:81306.
- [20] Salamanca F, Georgescu M, Mahalov A, Moustaoui M, Martilli A. Citywide impacts of cool roof and rooftop solar photovoltaic deployment on near-surface air temperature and cooling Energy demand. Boundary Layer Meteorol 2016; 161: 203–21.
- [21] Lamaamar I, Tilioua A, Hamdi Alaoui MA. Thermal performance analysis of a poly csi PV module under semi-arid conditions. Mater Sci Energy Technol 2022; 5: 243–51.
- [22] Cortes A, Murashita Y, Matsuo T, Kondo A, Shimadera H, Inoue Y. Numerical evaluation of the effect of photovoltaic cell installation on urban thermal environment. Sustain Cities Soc 2015; 19: 250–8.
- [23] Dev M, Surabi M. Regional climate consequences of large-scale cool roof and photovoltaic array deployment. Environ Res Lett 2011; 6:034001.
- [24] Barron-Gafford GA, Minor RL, Allen NA, Cronin AD, Brooks AE, Pavao-Zuckerman MA. The photovoltaic heat island effect: larger solar power plants increase local temperatures. Sci Rep 2016; 6: 1–7.
- [25] Garshasbi S, Khan A, Santamouris M. On the cooling energy penalty of urban photovoltaics: a case study in Sydney, Australia. Energy Build 2023; 294:113259.
- [26] Khan A, Santamouris M. On the local warming potential of urban rooftop photovoltaic solar panels in cities. Sci Rep 2023; 13: 1–19.
- [27] Khan A, Anand P, Garshasbi S, Khatun R, Khorat S, Hamdi R, et al. Rooftop photovoltaic solar panels warm up and cool down cities. Nat Cities 2024; 1(11):780–90.
- 28] Von Schuckmann K, Palmer MD, Trenberth KE, Cazenave A, Chambers D, Champollion N, et al. An imperative to monitor Earth's energy imbalance. Nat Clim Chang 2016; 6(2):138–44.

- [29] Elhabodi TS, Yang S, Parker J, Khattak S, He BJ, Attia S. A review on BIPV-induced temperature effects on urban heat islands. Urban Clim 2023: 50:101592.
- [30] Akbari H, Menon S, Rosenfeld A. Global cooling: increasing world-wide urban albedos to offset CO₂. Clim Change 2009; 94: 275–86.
- [31] Xu Z, Li Y, Qin Y, Bach E. A global assessment of the effects of solar farms on albedo, vegetation, and land surface temperature using remote sensing. Sol Energy 2024; 268:112198
- [32] Burg BR, Ruch P, Paredes S, Michel B, Burg BR, Ruch P, et al. Placement and efficiency effects on radiative forcing of solar installations. in: AIP Conference Proceedings; vol. 1679, 2015.
- [33] Akbari H, Damon Matthews H, Seto D. The long-term effect of increasing the albedo of urban areas. Environ Res Lett 2012; 7:024004.
- [34] Hu A, Levis S, Meehl GA, Han W, Washington WM, Oleson KW, et al. Impact of solar panels on global climate. Nat Clim Chang 2015; 6: 290–4.
- [35] Nemet GF. Net radiative forcing from widespread deployment of photovoltaics. Environ Sci Technol 2009; 43: 2173–8.
- [36] Baldridge AM, Hook SJ, Grove CI, Rivera G. The ASTER spectral library version 2.0. Remote Sens Of Environ 2009; 113: 711–5.
- [37] Gueymard CA. Parameterized transmittance model for direct beam and circumsolar spectral irradiance. Sol Energy 2001 10; 71(5):325–46.
- [38] Ziar H, Sönmez FF, Isabella O, Zeman M. A comprehensive albedo model for solar energy applications: geometric spectral albedo. Appl Energy 2019; 255:113867.
- [39] Ecosystem unit map | CBS. [Online]. Available: https://www.cbs.nl/en-gb/background/2017/12/ecosystem-unit-map
- [40] SMARTS: simple model of the atmospheric radiative transfer of sunshine | grid modernization | NREL. [Online]. Available: https://www.nrel.gov/grid/solar-resource/smarts.html
- [41] Gueymard CA. SMARTS2, a simple models of the atmospheric radiative transfer of sunshine. Florida Solar Energy Center; 1995. [Online]. Available: http://www. solarconsultingservices.com/publication.php
- [42] Meteonorm Version 8-Meteonorm (en). [Online]. Available: https://meteonorm. com/en/meteonorm-version-8
- [43] Asphalt and road construction in the Netherlands | TNO. [Online]. Available: https://www.tno.nl/en/sustainable/infrastructure/asphalt/
- [44] Schelhaas M, Clerkx APPM. State of the forests in the Netherlands, 2012-2013. 2014. [Online]. Available: https://research.wur.nl/en/publications/state-ofthe-forests-in-the-netherlands-2012-2013
- [45] LAMBDA 1050+ UV/Vis/NIR spectrophotometer | PerkinElmer. [Online]. Available: https://www.perkinelmer.com/product/lambda-1050-2d-base-inst-no-sw-l6020055
- [46] Leusink J. The future of the Dutch national height model (AHN). Point Cloud Process Symp 2018. [Online]. Available: https://3d.bk.tudelft.nl/pdfs/pcp2018/pcp2018_ JeroenLeusink.pdf
- [47] AHN 4 | Actuel Hoogtebestand Nederland. [Online]. Available: https://www.ahn. nl/ahn-4
- [48] Vo AV, Laefer DF, Smolic A, Zolanvari SMI. Per-point processing for detailed urban solar estimation with aerial laser scanning and distributed computing. ISPRS J Photogramm Remote Sens 2019; 155: 119–35.
- [49] Gupta MK, Bumtariya KJ, Shukla HA, Patel P, Khan Z. Methods for evaluation of radiation view factor: a review. Mater Today Proc 2017; 4: 1236–43.
- [50] Wang Z, Schaaf C, Lattanzio A, Carrer D, Grant I, Román M, et al. Global surface albedo product validation best practices protocol. Version 1.0. NASA, Tech. Rep., 2019.
- [51] Gadelmawla ES, Koura MM, Maksoud TMA, Elewa IM, Soliman HH. Roughness parameters. J Mater Process Technol 2002; 123: 133–45.
- [52] Aida M. Urban albedo as a function of the urban structure—a model experiment—Part I. Boundary Layer Meteorol 1982; 23(4):405–13.
- [53] Calcabrini A, Ziar H, Isabella O, Zeman M. A simplified skyline-based method for estimating the annual solar energy potential in urban environments. Nat Energy 2019; 4(3):206–15.
- [54] Home-Basisregistratie Adressen en Gebouwen (BAG). [Online]. Available: https://bag.basisregistraties.overheid.nl/
- [55] Zhou Y, Wilmink D, Zeman M, Isabella O, Ziar H. A geographic information systembased large scale visibility assessment tool for multi-criteria photovoltaic planning on urban building roofs. Renew Sustain Energy Rev 2023; 188:113885.
- [56] Keijzer MC. A multi-surface reflected irradiance model for pyranometer corrections and PV yield calculations in complex urban geometries. Delft University of Technology, Tech. Rep., 2019. [Online]. Available: http://repository.tudelft.nl/
- [57] de Vries TNC, Bronkhorst J, Vermeer M, Donker JCB, Briels SA, Ziar H, et al. A quick-scan method to assess photovoltaic rooftop potential based on aerial imagery and LiDAR. Sol Energy 2020; 209: 96–107.
- [58] Wohlfahrt G, Tomelleri E, Hammerle A. The albedo-climate penalty of hydropower reservoirs. Nat Energy 2021; 6: 372–7.
- [59] Bright RM, O'Halloran TL. A monthly shortwave radiative forcing kernel for surface albedo change using CERES satellite data. 2019.
- [60] Bright R, O'Halloran T. Developing a monthly radiative kernel for surface albedo change from satellite climatologies of Earth's shortwave radiation budget: CACK v1.0. Geosci Model Dev 2019; 12: 3975–90.
- [61] Wohlfahrt G, Tomelleri E, Hammerle A. The albedo-climate penalty of hydropower reservoirs. [Online]. Available: https://zenodo.org/records/4432576
- [62] Bright RM, Bogren W, Bernier P, Astrup R. Carbon-equivalent metrics for albedo changes in land management contexts: relevance of the time dimension. Ecol Appl 2016; 26: 1868–80.
- [63] CO₂ emissions from fuel combustion | OECD iLibrary. [Online]. Available: https: //www.oecd-ilibrary.org/energy/co2-emissions-from-fuel-combustion_22199446

[64] Joos F, Roth R, Fuglestvedt JS, Peters GP, Enting IG, Von Bloh W, et al. Carbon dioxide and climate impulse response functions for the computation of greenhouse gas metrics: a multi-model analysis. Atmos Chem Phys 2013; 13: 2793–825.

- [65] MODIS/Terra+Aqua BRDF/Albedo model parameters daily L3 global-500 m-LAADS DAAC. [Online]. Available: https://ladsweb.modaps.eosdis.nasa.gov/ missions-and-measurements/products/MCD43A1#overview
- [66] Wang S, Trishchenko AP, Sun X. Simulation of canopy radiation transfer and surface albedo in the EALCO model. Clim Dyn 2007; 29: 615–32.
- [67] Blakesley JC, Koutsourakis G, Parsons DE, Mica NA, Balasubramanyam S, Russell MG. Sourcing albedo data for bifacial PV systems in complex landscapes. Sol Energy 2023: 266:112144.
- [68] Sobrino JA, Franch B, Oltra-Carrió R, Vermote EF, Fedele E. Evaluation of the MODIS albedo product over a heterogeneous agricultural area. Int J Remote Sens 2013; 34(15):5530–40.
- [69] Coddington O, Schmidt KS, Pilewskie P, Gore WJ, Bergstrom RW, Román M, et al. Aircraft measurements of spectral surface albedo and its consistency with ground-based space-borned observations. J Geophys Res 2008 9; 113(17):17209.
- [70] Yan K, Li H, Song W, Tong Y, Hao D, Zeng Y, et al. Extending a linear kernel-driven BRDF model to realistically simulate reflectance anisotropy over rugged terrain. IEEE Trans Geosci Remote Sens 2022; 60.

- [71] Lacis AA. Albedo Feedbacks. In Gornitz V, editor. Encyclopedia of paleoclimatology and ancient environments. Dordrecht: Springer Netherlands; 2009. pp. 2–4. [Online]. Available: https://doi.org/10.1007/978-1-4020-4411-3_2
- [72] Wetter und Klima-Deutscher Wetterdienst-Climate maps Europe-Surface albedo-Monthly values. [Online]. Available: https://www.dwd.de/EN/ourservices/rcccm/ int/rcccm.int.sal.html?nn=790954
- [73] Boers R, Bosveld F, Klein Baltink H, Knap W, Van Meijgaard E, Wauben W. Observing and modelling the surface radiative Budget and cloud radiative forcing at the Cabauw Experimental Site for Atmospheric Research (CESAR), the Netherlands, 2009–17. J Clim 2019; 32(21):7209–25.
- [74] Ortiz Lizcano JC, Villa S, Zhou Y, Frantzi G, Vattis K, Calcabrini A, et al. Optimal design of multilayer optical color filters for building-integrated photovoltaic (BIPV) applications. Sol RRL 2023;(19):2300256.
- [75] Reichel C, Müller A, Friedrich L, Herceg S, Mittag M, Neuhaus DH. CO₂ emissions of silicon photovoltaic modules-impact of module design and production location. in: WCPEC-8, 8th World Conference on Photovoltaic Energy Conversion; 2022